JOURNAL OF COMPUTATIONAL PHYSICS **128,** 197–208 (1996)
ARTICLE NO. 0203

Basis Spline Collocation Method for Solving the Schrödinger Equation in Axillary Symmetric Systems

D. R. KEGLEY JR.,*,† V. E. OBERACKER,*,† M. R. STRAYER,* A. S. UMAR,*,† AND J. C. WELLS*,‡

*Center for Computationally Intensive Physics, Physics Division, Oak Ridge National Laboratory, Oak Ridge, Tennessee 37831-6373; †Vanderbilt University, Department of Physics and Astronomy, Nashville, Tennessee 37235; ‡Harvard-Smithsonian Center for Astrophysics, 60 Garden St., Cambridge, Massachusetts 02138

Received January 19, 1996; revised May 6, 1996

We use basis spline collocation to solve the Schrödinger equation on a lattice for axially symmetric systems, with and without spin. The focus of the present work is on systems which have continuum states, weakly bound states, or strong spin–orbit coupling, since these are the most difficult to solve on the lattice. A brief overview of the basis spline collocation method is included which concentrates primarily on those aspects of the theory which are relevant to its application in cylindrical coordinates. To demonstrate the method, we solve several model problems selected from the fields of atomic and nuclear physics.

I. INTRODUCTION

The increasing recognition of the utility of B-splines is evidenced by the fact that spline theory is now included in introductory texts [1] on numerical analysis. Even today, however, most of the literature concerning splines emphasizes their use for approximation and interpolation [2–4]. Although the B-spline collocation method (BSCM) for solving differential equations has been well described [5, 6] and in use for some time [7], it has not enjoyed the same level of general acceptance as other spline techniques for scientific applications. This may be due, in part, to the fact that the elegant structure of the theory is somewhat obscured when the method is applied to noncartesian coordinate systems.

The theory underlying BSCM in one dimension can be expressed quite compactly using matrix–vector notation, as pointed out in Ref. [8]. The inclusion of array processing features in modern programming languages [9] allows this conceptual simplicity to be reflected in the actual programming of the BSCM. Further, this direct correlation with the theory remains evident, even when the method is applied to systems with two or more dimensions and noncartesian coordinates.

Our interest in this area arises from the problem of modeling short lived nuclei in which the Fermi levels are near the continuum. The development of an appropriate theoretical treatment for this type of system has proven to be difficult [10]. B-splines are well suited to this task for a number of reasons. They have excellent interpolating properties, nonlinear grids may be used to represent novel phenomena, and continuum states can be treated in a realistic manner [11].

The methods which we are considering are not specific to the field of nuclear physics. Indeed, the modeling of heat conduction and fluid flow around cylindrical barriers were among the first serious applications of the BSCM in more than one dimension [12]. Several physical systems of current interest, such as the behavior of atoms in strong electromagnetic fields [13], have cylindrical symmetry and will benefit from accurate numerical approaches.

In Section II we briefly review the rudiments of the BSCM, emphasizing the matrix–vector notation. We also outline a method for enumerating the B-splines and collocation points which is appropriate for the axial grid. In Section III we examine the kinetic energy spectrum of a single particle in a cylindrical exposure. In addition to the usual uniform knot spacing, we also investigate the use of highly skewed knot distributions. In Section IV we implement the Morse potential problem on a cylindrical grid with a highly nonlinear knot spacing to demonstrate the effectiveness of BSCM for modeling weakly bound systems. Finally, the method is applied to a deformed oscillator with spin–orbit coupling in Section V.

II. BASIS SPLINE COLLOCATION

In this section we will review some of the features of the BSCM and show how the method can be applied to axially symmetric systems. Applications of the method in Cartesian coordinates and in spherical coordinates, for systems with spherical symmetry, can be found in Ref. [8]. We preface the section by pointing out that the method

0021-9991/96 $18.00

which we use to allocate the collocation grid is slightly different from that which was presented in Ref. [8]. We have found that the use of redundant boundary conditions, in conjunction with nonlinear grids and high order interpolation, may lead to poorly conditioned systems of equations. Therefore, the grid generation scheme which we present here utilizes extra internal data points rather than redundant boundary conditions.

A. *Representation of Functions and Operators*

A one dimensional physical region is partitioned into N segments by a set of $N + 1$ points $\{x_i\}$ known as *knots.* Unevenly spaced and multiply-defined knot locations are allowed, but the sequence of elements must be arranged in nondescending order. Thus the largest and smallest elements in the set ($x_{\max}$ and $x_{\min}$) correspond to the boundaries of the physical region. A set of interpolating spline functions with order M, $\{B_i^M(x)\}$, is constructed and each spline is indexed according to its location within the partitioned region. The ith B-spline vanishes outside the interval (x_i, x_{i+M}) and is constructed from piecewise continuous polynomials which are required to match at the knot locations within the interval. Each of the splines has continuous derivatives through the $(M-2)^{\text{th}}$ order and a discontinuous $(M-1)^{\text{th}}$ derivative. In actual calculations nonzero B-splines and nonvanishing derivatives are generated by recursion relations.

To guarantee that the splines generated on the knot sequence obey the completeness relation,

$$\sum_i B_i^M(x) = 1, \tag{1}$$

we form an extended partition by adding $M-1$ extra segments to each end of the grid. Restricting these extra segments to zero length (multiply defined knots at the endpoints) ensures that the analytical quadrature relation,

$$\int_{x_{\min}}^{x_{\max}} B_i^M(x)\,dx = \frac{x_{i+M} - x_i}{M}, \tag{2}$$

can be applied everywhere within the physical region, including the boundaries. The resulting knot sequence is

$$\text{knot sequence} = (\underbrace{x_1, x_2, ..., x_M}_{=x_{\min}}, x_{M+1}, ..., x_{M+N-1}, \underbrace{x_{M+N}, ..., x_{N+2M-1}}_{=x_{\max}}). \tag{3}$$

The number of splines in the basis ($\mathcal{N}$) is thus determined by the number of segments in the physical region and the spline order,

$$\mathcal{N} = N + M - 1. \tag{4}$$

Each spline is numbered sequentially as indicated in Fig. 1.

An arbitrary function $f(x)$ can be approximated as an expansion on the spline basis,

$$f(x) = \sum_{i=1}^{\mathcal{N}} B_i^M(x) c^i. \tag{5}$$

Collocation points $\{x_\alpha\}$ are placed at the location of each spline maximum within the interior of the physical region. This is accomplished by a simple binary search for the zeros of the first derivatives. Although the method is rather time consuming, it only needs to be performed once at the beginning of each calculation. Further, this method offers several advantages. First, it increases the magnitude of the diagonal elements in the resulting linear equations. This in turn gives a system which is better conditioned for subsequent numerical work. Second, it can be easily automated. Finally, this scheme is valid for nonuniform knot spacings and it permits the addition of extra collocation points within the interior to accommodate splines of higher order.

The total number of collocation points is given by

$$n = \mathcal{N} - 2. \tag{6}$$

The collocation formalism requires that the expansion coefficients be selected so that Eq. (5) is exactly satisfied at the collocation points. It is convenient to define elements of a vector $f_\alpha \equiv f(x_\alpha)$ and a matrix $B_{\alpha i} \equiv B_i^M(x_\alpha)$, and express the relation in matrix–vector notation

$$(\mathbf{f})_n = (\mathbf{B})_{n\times\mathcal{N}}(\mathbf{c})_{\mathcal{N}}. \tag{7}$$

To solve for the expansion coefficients we incorporate homogeneous boundary conditions,

$$\sum_{p\geq 0} K_p \frac{d^p}{dx^p} f(x)\bigg|_{\text{boundary}} = \sum_{p\geq 0} K_p \frac{d^p}{dx^p} \sum_{i=1}^{\mathcal{N}} B_i^M(x)\bigg|_{\text{boundary}} c^i = 0. \tag{8}$$

Two row vectors whose elements have the form

$$\beta_i \equiv \sum_{p\geq 0} K_p \left[\frac{d^p}{dx^p} B_i^M(x)\right]_{\text{boundary}} \tag{9}$$

are evaluated at the left (L) and right (R) ends of the grid, and an augmented coefficient matrix is then constructed,

$$\tilde{\mathbf{B}} \equiv \begin{pmatrix} \mathbf{B} \\ \beta^{\text{L}} \\ \beta^{\text{R}} \end{pmatrix}_{\mathcal{N}\times\mathcal{N}}. \tag{10}$$

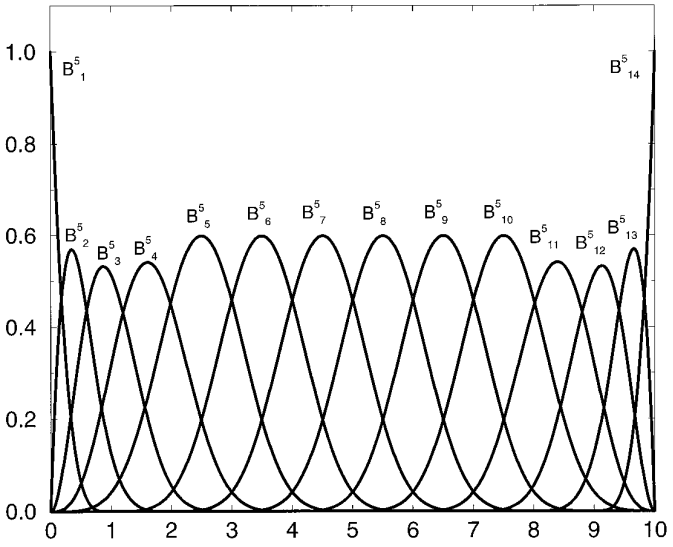

FIG. 1. Depicted is a set of fifth-order splines constructed on 10 uniform-length knot segments in the physical region. Extra zero-length segments are appended to each end of the grid so that the splines form a complete basis on the physical interval.

This method of assigning elements in $\tilde{\mathbf{B}}$ ensures that the matrix is nonsingular [3], even with nonuniform grids, so Eq. (7) can be inverted:

$$(\mathbf{c})_{\mathcal{N}} = (\tilde{\mathbf{B}}^{-1})_{\mathcal{N}\times\mathcal{N}} \begin{pmatrix} \mathrm{f} \\ \hline 0 \\ 0 \end{pmatrix}_{\mathcal{N}}. \tag{11}$$

The inverse matrix is used to generate collocation matrix operators which automatically satisfy the desired boundary conditions. However, due to the presence of zeroes in the column vector, only a portion of the inverse matrix is actually required. We denote that portion by

$$(\tilde{\mathbf{C}})_{\mathcal{N}\times n}, \tag{12}$$

and we note that it satisfies the relation

$$\sum_i B_{\alpha i}\tilde{C}^{i\beta} = \delta_\alpha^\beta. \tag{13}$$

Just as functions are represented as vectors in collocation space, operators are represented as matrices. Consider the action of an operator $\mathcal{O}$ on a function $f(x)$:

$$\mathcal{O}f(x) = \sum_i [\mathcal{O}B_i^M(x)]c^i. \tag{14}$$

The collocation representation is constructed by evaluating the operator's action at the collocation points and substituting from Eq. (11) for the expansion coefficients. The resulting transformation becomes

$$\mathcal{O}f(x) \to [\mathcal{O}f]_\alpha = \sum_\beta O_\alpha^\beta f_\beta = (\mathbf{O})_{n\times n}(\mathbf{f})_n. \tag{15}$$

The matrix elements O_α^β are evaluated explicitly as

$$O_\alpha^\beta = \sum_i [\mathcal{O}B_i^M(x_\alpha)][\tilde{C}]^{i\beta}. \tag{16}$$

Thus, in one dimension the operation is reduced to matrix multiplication, and the evaluation of the matrix elements does not require a priori knowledge of the function.

The generalization of higher dimensions is straightforward. The function is represented as a simple array with the appropriate number of dimensions, and partial differential operators become square matrices which act only on one dimension. Two-dimensional spatial arrays are especially convenient since all operations can be implemented with simple matrix multiplication and transposition.

B. *Representation of the Schrödinger Equation for Axially Symmetric Systems*

For axially symmetric systems without spin, the angular dependence may be separated so that eigenfunctions of the Hamiltonian have the form

$$\psi(r, \varphi, z) = \frac{e^{i\mu\varphi}}{\sqrt{2\pi}} f(r, z), \tag{17}$$

where r and z are distances measured perpendicular and parallel to the symmetry axis, φ is the azimuthal angle, and μ represents the projection of the orbital angular momentum onto the symmetry axis which is a constant of the motion. The equation which must be solved on the grid is

$$-\frac{\hbar^2}{2m}\left(\frac{\partial^2 f}{\partial r^2} + \frac{1}{r}\frac{\partial f}{\partial r} - \frac{\mu^2}{r^2}f + \frac{\partial^2 f}{\partial z^2}\right) + V(r, z)f = Ef. \tag{18}$$

To implement this with BSCM we define the knots and collocation points and construct partial derivative operators for each dimension using the method outlined in Section II.A. The numbers of collocation points in the r and z directions are denoted by n_r and n_z, respectively.

The function and the potential are represented as $n_r \times n_z$ arrays, $f_{\alpha\beta}$ and $\mathbf{V}_{\alpha\beta}$. Two $n_r \times n_r$ diagonal matrices are constructed to represent the explicit r terms on the left side of Eq. (18), $(1/r_\alpha)_{\text{diag}}$ and $(\mu^2/r_\alpha^2)_{\text{diag}}$. Partial derivative operators are denoted by $\mathbf{D}_x^p$, where the superscript specifies the order of the derivative and the subscript indicates the direction. It is convenient to separate the kinetic energy into contributions from each dimension,

$$\mathbf{R}_{n_r \times n_r} = -\frac{\hbar^2}{2m}\left(\mathbf{D}_r^2 + (1/r_\alpha)_{\text{diag}}\,\mathbf{D}_r^1 - (\mu^2/r_\alpha^2)_{\text{diag}}\right) \quad (19)$$

and

$$\mathbf{Z}_{n_z \times n_z} = -\frac{\hbar^2}{2m}(\mathbf{D}_z^2). \quad (20)$$

Equation (18) becomes

$$\sum_{\alpha'} \mathbf{R}_{\alpha\alpha'} f_{\alpha'\beta} + \sum_{\beta'} \mathbf{Z}_{\beta\beta'} f_{\alpha\beta'} + \mathbf{V}_{\alpha\beta} f_{\alpha\beta} = E f_{\alpha\beta}, \quad (21)$$

or in matrix–vector notation,

$$\mathbf{Rf} + \mathbf{fZ}^{\mathrm{T}} + \mathbf{V} * \mathbf{f} = E * \mathbf{f}. \quad (22)$$

In this notation juxtaposition indicates normal matrix multiplication, the superscript T is transposition, and the symbol $*$ represents element by element multiplication of conformable arrays. Scalars quantities, such as E, are assumed to be conformable to any array.

It should be noted that the spatial resolution of the collocation grid imposes some restrictions on the physical interpretation of the numerical results. Several factors must be considered. First, the largest magnitude of momentum which can be faithfully represented on the grid is fundamentally limited by the *Nyquist* criterion [14],

$$|p|_{\max} \leq \frac{\hbar\pi}{\Delta}, \quad (23)$$

where Δ is the largest separation between adjacent collocation points. With nonlinear grid spacings, some of the numerically calculated energy eigenstates will correspond to momenta above this limit. Since the r and z contributions to the kinetic energy are independent, the limit applies to both dimensions. For the examples we are considering, it is computationally efficient to define the collocation grid so that the limiting spatial resolutions in both directions are roughly equal. Finally, the quality of the spline approximation generally depends on the interpolating order of the basis and on the length of the knot segments [6]. We have found empirically (with one-dimensional calculations of kinetic energy eigenvalues) that the relative error in the calculated eigenvalues increases gradually with the energy. To mitigate the effect of this type of error in actual calculations we may refine the grid spacing and check for convergence.

C. *Solution by Direct Diagonalization*

One important advantage of the BSCM is the reduction in computational effort which arises from the excellent interpolating properties of the B-splines. A viable option (for two-dimensional problems) is to construct an explicit single matrix representation of the Hamiltonian and to solve the eigenvalue problem by direct factorization. The f array is mapped column by column into a large vector, and the corresponding Hamiltonian matrix ($\mathbf{H}$) is constructed.

$$f_{\alpha\beta} \rightarrow f_k \quad (24)$$

$$\{\mathbf{R}_{\alpha\alpha'}, \mathbf{Z}_{\beta\beta'}, \mathbf{V}_{\alpha\beta}\} \rightarrow \mathbf{H}_{kk'}. \quad (25)$$

The specific mapping which will accomplish this is

$$k = (\beta - 1)n_r + \alpha \quad (26)$$

$$k' = (\beta' - 1)n_r + \alpha'. \quad (27)$$

The solution is obtained by applying a Schur factorization [15] to decompose $\mathbf{H}$.

It has been observed that the collocation representation of an Hermitian operator is not necessarily an Hermitian matrix [16, 17]. This is a special concern in our case due to the nonlinear spacing of the data points and the presence of the $1/r_\alpha$ term. In the present calculations eigenvalues are sorted into ascending order and states above the Nyquist limit are discarded. The appearance of an imaginary component among the remaining states is interpreted as an error condition. Such errors are rare in actual calculations. For time independent problems such as those being considered in the present work, the loss of symmetry in the Hamiltonian represents a mere inconvenience. However, for the time-dependent Schrödinger equation this problem can be quite serious. In some instances it is possible to restore the required symmetry by judicious choice of grid points and boundary conditions, but in general the BSCM as it is currently formulated is not well suited for the time dependent problem. We will specifically address the issue of Hermitian operators in future work.

III. KINETIC ENERGY SPECTRUM

The first test case which we consider is the kinetic energy spectrum of a single particle on the two-dimensional grid. For simplicity, Eq. (18) is expressed in natural units ($\hbar = m = c = 1$),

$$-\frac{\partial^2 f}{\partial r^2}-\frac{1}{r}\frac{\partial f}{\partial r}+\frac{\mu^2}{r^2}f-\frac{\partial^2 f}{\partial z^2}=2\mathscr{E}f, \tag{28}$$

where $\mathscr{E}$ is the energy measured in units of mc^2. This imposes a characteristic length scale which is equivalent to measuring distance in units of the reduced Compton wavelength ($\lambda\!\!\!^{-}_c = \hbar/mc$). We define the grid so that the physical region extends equal distances in both the plus and minus z directions. The edges of the grid represent an impenetrable cylindrical enclosure. Obviously, f must be required to vanish at $r_{\max}$ and $\pm z_{\max}$. There is also a physical requirement that solution wavefunctions be differentiable everywhere inside of the enclosure which imposes restrictions on the behavior of $f(r, z)$ near the symmetry axis. Since spin is not included, the boundary conditions will depend only on the quantum number μ,

$$f(r,z)\big|_{r=0}=0, \quad \mu=\text{odd}, \tag{29}$$

$$\left.\frac{\partial f}{\partial r}\right|_{r=0}=0, \quad \mu=\text{even}. \tag{30}$$

Separation of variables gives the kinetic energy eigenvalues

$$\mathscr{E}_{\mu,n,k}=\frac{1}{2}\left(\frac{\nu_{n,\mu}^2}{r_{\max}^2}+\frac{k^2\pi^2}{4z_{\max}^2}\right), \tag{31}$$

where $\nu_{n,\mu}$ is the nth zero of the Bessel function $J_\mu(x)$.

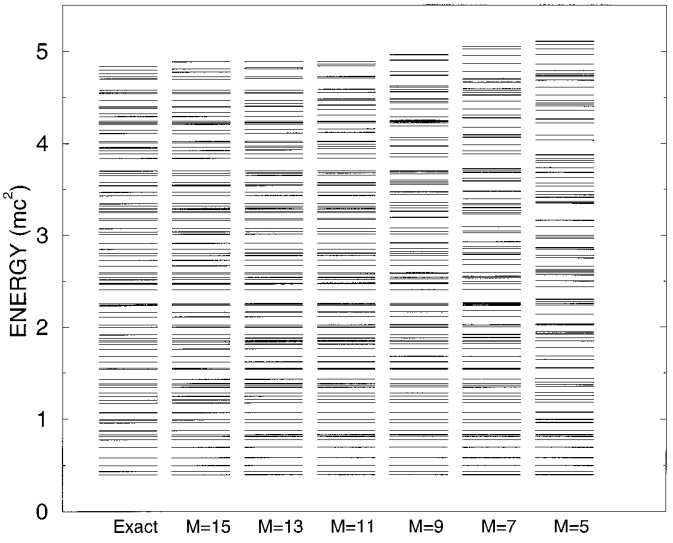

FIG. 2. Kinetic energy eigenvalues for a particle within a cylindrical enclosure, having angular momentum projection $\mu = 5$. The B-splines used for the calculation are constructed on a collocation grid with $r_{\max} = |\pm z_{\max}| = 10\lambda\!\!\!^{-}_c$, knots are distributed uniformly at 1 $\lambda\!\!\!^{-}_c$ intervals. Data corresponding to the 20 highest levels are given in Table I. M represents the spline order.

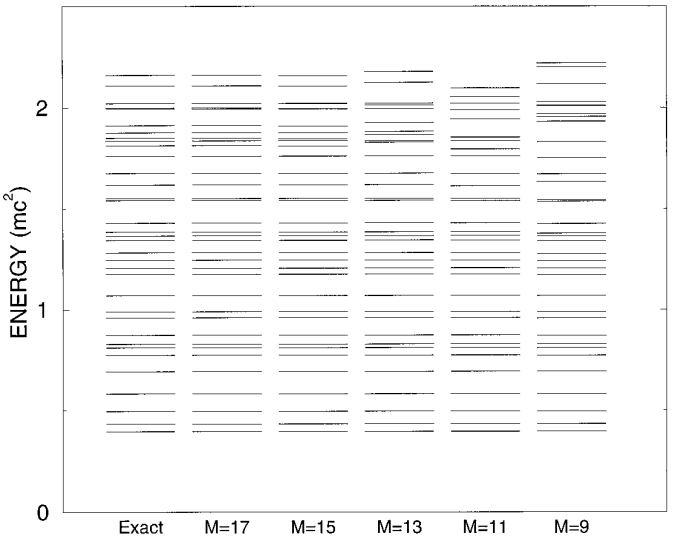

FIG. 3. Kinetic energy eigenvalues for a particle within a cylindrical enclosure, having angular momentum projection $\mu = 5$. The B-splines used for the calculation are constructed on a collocation grid with $r_{\max} = |\pm z_{\max}| = 10\lambda\!\!\!^{-}_c$, knots are distributed nonuniformly as described in the text. M represents the spline order.

A. *Linear Knot Distribution*

For our present numerical calculations we fix the grid boundaries at $10\lambda\!\!\!^{-}_c$. Initially, the knots are uniformly spaced at one unit intervals in both the r and z directions. Splines of various orders are constructed on this grid and the eigenvalues of the corresponding Hamiltonian operator are found by the method in Section II.C. Figure 2 shows that the higher order splines reproduce the general structure of the analytical spectrum. Numerical results corresponding to the 20 highest levels are also given in Table I. No assumption of separability is made in the numerical calculations so it is interesting to note that these results agree to 15 significant digits with the results obtained when the r and z equations are separated and solved on one-dimensional grids in double precision.

B. *Nonlinear Knot Distribution*

Our next test involves the same physical region but with a different gridding scheme. In order to simulate the behavior of the kinetic energy operator in conjunction with an interaction which is strongly concentrated near the origin, the knot locations in both dimensions are distributed according to the relation

$$|x_i| = e^{\Lambda\zeta_i^2} - 1, \tag{32}$$

where $\Lambda = \log(x_{\max})$ and the ζ's are uniformly distributed on the interval (0, 1). This gives a high density of collocation points near the origin but allows the grid to extend

TABLE I

Kinetic Energy Eigenvalues for a Particle in a Cylindrical Enclosure

Level	Eigenvalue	$M = 15$	$M = 13$	$M = 11$	$M = 9$	$M = 7$	$M = 5$
81	4.1097	4.1085	4.1123	4.1214	4.1887	4.2723	4.4050
82	4.1467	4.1456	4.1493	4.1584	4.2257	4.2733	4.4268
83	4.2084	4.2072	4.2110	4.2201	4.2342	4.2735	4.4275
84	4.2192	4.2195	4.2201	4.2228	4.2458	4.2830	4.4400
85	4.2328	4.2327	4.2329	4.2337	4.2504	4.3105	4.4645
86	4.2446	4.2446	4.2447	4.2454	4.2874	4.3722	4.5262
87	4.2948	4.2936	4.2973	4.3065	4.3738	4.4586	4.6127
88	4.3266	4.3370	4.3489	4.3702	4.4367	4.5191	4.6868
89	4.3818	4.3941	4.4003	4.4132	4.4494	4.5321	4.7239
90	4.3907	4.3992	4.4084	4.4175	4.4804	4.5526	4.7373
91	4.4058	4.4046	4.4335	4.4682	4.4848	4.5696	4.7375
92	4.4672	4.4671	4.4673	4.4825	4.5625	4.5951	4.7563
93	4.5415	4.5403	4.5441	4.5532	4.5846	4.6651	4.7927
94	4.5531	4.5531	4.5533	4.5546	4.6083	4.6966	4.8604
95	4.5770	4.5779	4.5799	4.5869	4.6205	4.7054	4.8604
96	4.7019	4.7007	4.7045	4.7136	4.7401	4.7818	4.9657
97	4.7262	4.7262	4.7264	4.7273	4.7809	4.8659	5.0225
98	4.7583	4.7757	4.8100	4.8414	4.9041	4.9504	5.0718
99	4.7978	4.8083	4.8201	4.8590	4.9080	5.0244	5.1039
100	4.8383	4.8858	4.8869	4.8900	4.9611	5.0512	5.1088

Note. The collocation grid extends to $r_{\max} = |\pm z_{\max}| = 10\text{Å}_c$, knots are distributed uniformly at 1 Å$_c$ intervals in both dimension.

to very large distances. Despite the highly refined grid near the origin, the overall limiting spatial resolution is considerably lower than that obtained with uniform knot distributions. Corresponding to this reduced Nyquist limit, the energy cutoff level is also reduced.

All of the spline orders are able to reproduce the four lowest energy levels reasonably well, but splines of order 7 and below yield poor results at higher energies. Figure 3 shows a comparison of the calculated eigenvalues for the higher order splines. As the spline order is increased two trends are observed in the data. First, the calculated eigenvalues become more accurate. This can be attributed to the improved interpolating power of the higher order splines; the true solution is better approximated. Second, higher energy levels are obtained. This is related to the highly skewed knot distribution used in this example. Extra collocation points which are added near the boundaries to accommodate higher order splines, fall naturally into the region which has the poorest spatial resolution. Consequently, the Nyquist limit is substantially increased. This is quite distinct from the behavior of a grid with linear knot spacing, where the addition of a few extra collocation points has little effect on the overall spatial resolution. It is generally desirable to use high order interpolation with nonlinear knot distributions. However, the matrices which must be inverted to form the collocation space operators tend to become ill-conditioned.

The energy levels obtained with calculations based on this grid are sufficiently high to suggest that nonlinear distributions may offer a viable means for dealing with loosely bound states. In the next section we will use a variation of the knot distribution presented here for exactly this purpose.

IV. MORSE POTENTIAL WITH ROTATIONAL CORRECTION

The next case which we consider is to cast a radially symmetric potential problem in cylindrical coordinates. The Morse potential is often used to describe the vibrations of two-atom molecules. Denoting the radial distance from the origin as R, the potential can be expressed as

$$V(R) = V_0(e^{-2\alpha x} - 2e^{-\alpha x}), \quad x = \frac{R - R_0}{R_0}. \tag{33}$$

There are analytical solutions for the Schrödinger equation using this potential with no angular momentum, and it has been used as a test case for several studies [8, 16, 18]. The parameter set ($R_0 = 3$, $V_0 = 25$, $\alpha = 6$) duplicates the conditions used in Ref. [8]. There are four bound states corresponding to an orbital angular momentum of zero. The parameters were selected so that the highest bound state lies near the continuum. Due to the long exponential decay length associated with the highest bound state, it is difficult to perform accurate numerical calculations of the corresponding energy level. Therefore, this potential will

provide a demonstration of the use of B-splines for weakly bound systems.

Due to the fact that the axial calculations do not enforce conservation of total angular momentum, but only the z-component of the angular momentum, the energy level structure of the solution is more complicated. Besides the four $L = 0$ bound states, nonzero angular momentum states (up to $L = 18$) will also have bound states, each one giving rise to an extra $\mu = 0$ state. To deal with this fuller spectrum analytically we follow a method outlined in Ref. [19]. An asymptotic expansion of the centrifugal term is constructed about the potential minimum. This expansion has the same form as the original Morse potential. The effective potential (that is the original potential plus the centrifugal term) is approximated by a *rotationally corrected* Morse potential as illustrated in Fig. 4. The resulting energy levels are given by

$$\mathscr{E} = \frac{1}{2R_0^2}\left[-2R_0^2V_0 + 2\alpha\sqrt{2R_0^2V_0}\left(n+\frac{1}{2}\right) - \alpha^2\left(n+\frac{1}{2}\right)^2 + l(l+1) - \frac{9(\alpha-1)^2}{4\alpha^4\gamma^2}l^2(l+1)^2 - \frac{3(\alpha-1)}{\alpha\gamma}\left(n+\frac{1}{2}\right)l(l+1)\right]. \quad (34)$$

The first three terms correspond exactly to the analytical solution used in Ref. [8]. The fourth term is the rotational energy of a particle moving at a fixed radius of R_0. The fifth term accounts for the fact that the expectation value for the radius will vary with angular momentum. The last term represents the coupling between the rotational and vibrational modes of the system.

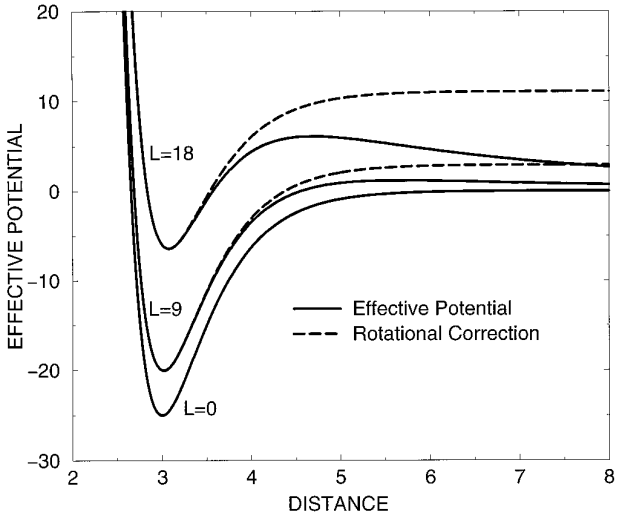

FIG. 4. Depicted are the representations of the ''effective potential'' (Morse potential plus centrifugal term) and the corresponding ''rotationally corrected'' potentials. The correction is accomplished by constructing an asymptotic expansion of the centrifugal term in the Hamiltonian about the location of the potential minimum. Since the approximation introduces a systematic upward shift to the energy for non-zero angular momenta, only $L = 0$ states are used for quantitative comparison.

Expressing the potential in cylindrical coordinates gives the actual expression which must be solved on the grid:

$$-\frac{1}{2}\left(\frac{\partial^2 f}{\partial r^2} + \frac{1}{r}\frac{\partial f}{\partial r} - \frac{\mu^2}{r^2}f + \frac{\partial^2 f}{\partial z^2}\right) + V_0\left[\exp\left(-2\alpha\frac{\sqrt{r^2+z^2}-R_0}{R_0}\right) - 2\exp\left(-\alpha\frac{\sqrt{r^2+z^2}-R_0}{R_0}\right)\right] = \mathscr{E}f. \quad (35)$$

Since we are concerned primarily with comparing solutions for the $L = 0$ states, we can restrict the numerical calculation to the positive quarter-plane and solve for even parity states. This is accomplished by setting a boundary condition in the equatorial plane,

$$\left.\frac{\partial f}{\partial z}\right|_{z=0} = 0. \quad (36)$$

The boundary conditions along all remaining boundaries are fixed in exactly the same manner as in the previous examples.

The collocation grid must have a relatively high density of points near the origin in order to accurately represent the potential near its minimum. At the same time, the grid must extend sufficiently far from the origin to cover the slow exponential decay of the highest bound state. These conflicting requirements are, in fact, the main difficulty with lattice calculations for weakly bound states. The requirements can be satisfied by constructing both the r and z grids in the following manner: the interval (0, 2) is assigned as a single knot segment; the remaining knots are assigned according to the mapping

$$x_i = x_{\min} + e^{\Lambda\zeta_i^2} - 1, \quad (37)$$

where $\Lambda = \log(x_{\max} - x_{\min})$ and the ζ's are uniformly distributed on the interval (0, 1). B-splines of order 17 were generated on this knot sequence and collocation points were allocated as described earlier.

The discretized Hamiltonian was solved by the method described in Section II.C and Fig. 5 provides a complete summary. The smooth curve represents the potential as a function of distance from the origin. Actual collocation points are indicated by closed circles. The level structure on the left was evaluated with Eq. (34); the four extended lines correspond to the four $L = 0$ bound states. The level

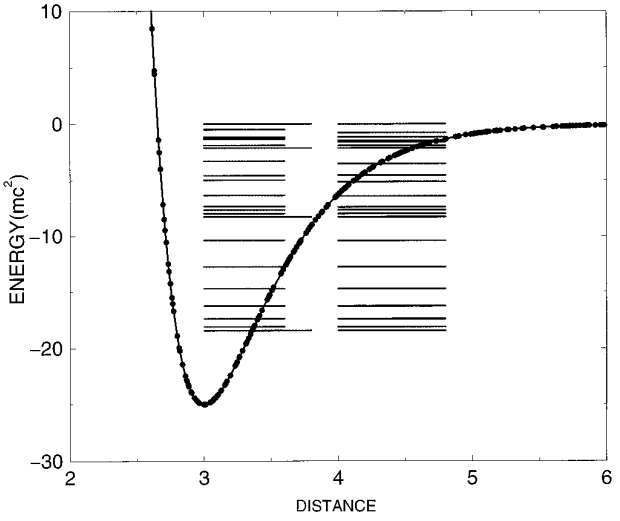

FIG. 5. Summary of results for the Morse potential problem. The smooth curve represents the potential as a function of distance from the origin, closed circles are actual data points. The figure depicts only the portion of the data points near the origin, the grid actually extended to more than $60\lambda_c$ with the point density becoming smaller at larger distances. Energy levels on the left were determined by the analytical formula given in the text (the four elongated lines correspond to $L = 0$ states, see Table II; those on the right were found with BSCM.

structure on the right was calculated with the BSCM. Both spectra show the same number of bound states with similar spacings between corresponding levels.

Table II shows the fractional error ($|E_{\text{Exact}} - E_{\text{Numerical}}|/|E_{\text{Exact}}|$) in the eigenvalues for the four $L = 0$ states. Also included are the results of a one dimensional calculation on a nonlinear grid using seventh-order splines from Ref. [8]. This should not be considered as a direct comparison since the grids on which these results are based are fundamentally different. Rather, the intention is to demonstrate that calculations on the cylindrical grid are in some sense competitive. The superior performance of the cylindrical calculation for the highest level can be attributed to the larger spatial distance covered and to the use of higher spline orders, which in turn is possible because of the slightly different scheme for allocating the collocation points. The lower accuracy of the low lying eigenvalues can also be easily understood; near the origin the radial calculation more fully exploits the natural symmetry of the Hamiltonian.

TABLE II

Fractional Error for $L = 0$ Bound States of the Morse Potential

Level	Eigenvalue	Axial grid	Radial grid
1	−18.428932	4.4E-05	5.4E-08
2	−8.2867966	1.4E-04	1.6E-05
3	−2.1446609	1.8E-04	1.3E-04
4	−0.0025253	8.9E-03	3.9E-1

Note. Axial calculations were carried on a 2-d grid representing the positive quarter-plane in r and z. The grid extends to 60 λ_c in each direction using a nonlinear knot distribution described in the text. Radial calculations are taken from Ref. [8].

Having made the case that nonlinear grids can be used to improve the effectiveness of BSCM for modeling weakly bound states, some caveats are in order; we do not intend to imply that such measures are always appropriate. Indeed, the numerical results in Section III and the subsequent discussion indicate that the contribution from the kinetic energy operator to high lying levels may be degraded by the introduction of nonlinear grids. Section III and the present section, when considered together, provide a pattern which can be used to assess whether a particular nonlinear grid is suitable. The nonlinear grid is only introduced into the potential problem after investigating the deleterious effects of comparable grid schemes on the raw kinetic energy operator. Model problems in these sections were specifically cast in a form with matching energy scales and characteristic lengths in order to facilitate this type of comparison. It should also be understood that the knot distribution defined in Eq. (37) is tailored to the Morse potential; other physical situations may require completely different grid schemes. In calculations with more realistic potentials (and also for self-consistent calculations where the effective potential evolves iteratively) we have found that it is more practical to compose a grid in several individual sections with each section having its own uniform spacing rather than trying to define an analytical distribution function.

V. DEFORMED OSCILLATOR

The final model system which we will treat is the deformed oscillator with spin–orbit coupling. In addition to testing the implementation of collocation space operators and boundary conditions, this also demonstrates the handling of spin degrees of freedom.

Under the assumption of axial symmetry we expect the z-projection of the *total* angular momentum to be a conserved quantity so that eigenstates of the Hamiltonian have the form

$$\psi = \psi_\Omega = \frac{1}{\sqrt{2\pi}} \begin{pmatrix} e^{i(\Omega-1/2)\varphi}\mathscr{U}(r,z) \\ e^{i(\Omega+1/2)\varphi}\mathscr{L}(r,z) \end{pmatrix}, \qquad \Omega = \pm\frac{1}{2}, \pm\frac{3}{2}, \pm\frac{5}{2}, \ldots, \tag{38}$$

where Ω represents the J_z quantum number, and the spatial functions $\mathscr{U}$ and $\mathscr{L}$ are assumed to be real.

In this example we follow the convention of using MeV for the unit of energy and fm for the unit of distance. An approximate value for the nucleon mass ($mc^2 = 939$ MeV) is used for all calculations. The Hamiltonian for the deformed oscillator becomes

$$\hat{H} = -\frac{\hbar^2}{2m}\left(\frac{\partial^2}{\partial r^2} + \frac{1}{r}\frac{\partial}{\partial r} + \frac{1}{r^2}\frac{\partial^2}{\partial \varphi^2} + \frac{\partial^2}{\partial z^2}\right) - V_0 + \frac{m}{2}(\omega_r^2 r^2 + \omega_z^2 z^2) - 2\hbar\omega_0 \kappa \mathbf{l}\cdot\mathbf{s}. \tag{39}$$

The oscillator frequencies are related to the frequency (ω_0) of a spherical oscillator, the mass number (A) of the system, and a small deformation parameter (δ), by the relations

$$\hbar\omega_0 = \frac{41}{A^{1/3}}\,(\text{MeV}) \tag{40}$$

$$\omega_r^2 = \omega_0^2\,(1 + \tfrac{2}{3}\delta) \tag{41}$$

$$\omega_z^2 = \omega_0^2\,(1 - \tfrac{4}{3}\delta). \tag{42}$$

This particular parameterization preserves the volume of the nucleus up to a small correction term in δ^2.

Casting all expressions explicitly in cylindrical coordinates yields a set of coupled equations for $\mathscr{U}$ and $\mathscr{L}$:

$$(\hat{T} + \hat{V} + \hat{H}_{\text{SO}}) \begin{pmatrix} \mathscr{U}(r,z) \\ \mathscr{L}(r,z) \end{pmatrix} = E \begin{pmatrix} \mathscr{U}(r,z) \\ \mathscr{L}(r,z) \end{pmatrix} \tag{43}$$

The potential depth and the number of nucleons were fixed at $V_0 = 50$ MeV and $A = 190$ for all calculations. The collocation grid was defined on a region extending from 0 fm to 15 fm in the r direction, and from -15 fm to $+15$ fm in the z-direction. Knots were distributed uniformly across the physical region in both directions at 1 fm intervals. The use of a nonlinear knot distribution in this example was not deemed appropriate since oscillator states, no matter how high the energy, are always tightly bound. B-spline bases of varying orders were constructed on the grid and eigenvalues of the Hamiltonian in Eq. (43) were obtained by a slight generalization of the method described in Section II.C. Boundary conditions were determined according to the same principles which were applied in the previous examples, but separate conditions are required for the upper and lower components of the spinor. These are summarized in Table III.

Validation of the program is carried out in several stages. For systems with no spin–orbit term ($\kappa = 0$), Eqs. (43) become uncoupled and can be solved by separation of variables. The analytical eigenvalues are given by the expression

$$E = \hbar\omega_z(\nu_z + \tfrac{1}{2}) + \hbar\omega_r(2\nu_r + |\mu| + 1) - V_0, \tag{47}$$

where the ν's represent the number of vibrational quanta in the r and z directions and $\mu = \Omega \pm \frac{1}{2}$. Thus, the first stage is to set $\kappa = 0$ and compare the results of numerical calculations with Eq. (47) for fixed deformation and angular momentum projection. Table IV shows a comparison

$$\hat{T} = -\frac{\hbar^2}{2m}\begin{pmatrix} \dfrac{\partial^2}{\partial r^2} + \dfrac{1}{r}\dfrac{\partial}{\partial r} - \dfrac{(\Omega - 1/2)^2}{r^2} + \dfrac{\partial^2}{\partial z^2} & 0 \\ 0 & \dfrac{\partial^2}{\partial r^2} + \dfrac{1}{r}\dfrac{\partial}{\partial r} - \dfrac{(\Omega + 1/2)^2}{r^2} + \dfrac{\partial^2}{\partial z^2} \end{pmatrix} \tag{44}$$

$$\hat{V} = \frac{m\omega_0^2}{2}\begin{pmatrix} r^2(1 + \tfrac{2}{3}\delta) + z^2(1 - \tfrac{4}{3}\delta) - \dfrac{2V_0}{m\omega_0^2} & 0 \\ 0 & r^2(1 + \tfrac{2}{3}\delta) + z^2(1 - \tfrac{4}{3}\delta) - \dfrac{2V_0}{m\omega_0^2} \end{pmatrix} \tag{45}$$

$$\hat{H}_{SO} = -\hbar\omega_0\kappa\begin{pmatrix} (\Omega - \frac{1}{2}) & -(\Omega + \frac{1}{2})\dfrac{z}{r} - z\dfrac{\partial}{\partial r} + r\dfrac{\partial}{\partial z} \\ -(\Omega - \frac{1}{2})\dfrac{z}{r} + z\dfrac{\partial}{\partial r} - r\dfrac{\partial}{\partial z} & -(\Omega + \frac{1}{2}) \end{pmatrix}. \tag{46}$$

TABLE III

Boundary Conditions along the z-Axis ($r = 0$)

Condition	Upper component boundary condition	Lower component boundary condition
$\Omega - \frac{1}{2} =$ even	$\partial_r \mathscr{U}\|_{r=0} = 0$	$\mathscr{L}\|_{r=0} = 0$
$\Omega - \frac{1}{2} =$ odd	$\mathscr{U}\|_{r=0} = 0$	$\partial_r \mathscr{L}\|_{r=0} = 0$

conducted at angular momentum projection $\Omega = \frac{3}{2}$ and deformation $\delta = 0.2$. The error values listed are representative of other calculations carried out at physically reasonable values for Ω and δ. The quality of the spline calculations is improved with increasing spline order. However, with the uniform knot distribution, little improvement is achieved by using splines of order higher than nine unless the knot distribution is also refined.

The second stage of validation is to check the spin–orbit splittings. In spherical coordinates the potential term in Eq. (39) can be expressed in terms of the spherical harmonic,

$$\frac{m}{2}(\omega_r^2 r^2 + \omega_z^2 z^2) = \frac{m}{2}\omega_0^2 (r^2 + z^2) \left[\left(1 - \frac{2}{3}\delta\right) + \frac{4}{3}\sqrt{\frac{4\pi}{5}}\,\delta Y_{20}(\theta, \varphi)\right]. \tag{48}$$

When there is no deformation, total angular momentum becomes a conserved quantity and the spin–orbit term can be diagonalized:

$$\mathbf{l}\cdot\mathbf{s} = \tfrac{1}{2}(j(j+1) - l(l+1) - \tfrac{3}{4}) = \begin{cases} \frac{1}{2}(j - \frac{1}{2}) & \text{for } l = j - \frac{1}{2}, \\ -\frac{1}{2}(j + \frac{3}{2}) & \text{for } l = j + \frac{1}{2}. \end{cases} \tag{49}$$

It is a straightforward process to identify which total angular momentum states can contribute to a given Ω state and to verify that each numerically calculated Ω eigenvalue corresponds to an appropriately shifted $\mathbf{J}^2$ eigenvalue. The results shown in Table V were generated by selecting a physically reasonable value ($\kappa = 0.05$) for the spin–orbit coupling for a spherically symmetric ($\delta = 0.0$) nucleus. Again, the results are consistent with the observation that the accuracy of the spine calculations improves with increasing spline order.

Except for the exclusion of a small orbital correction term in the potential, our deformed oscillator is identical to a standard model for the deformed nucleus known as the Nilsson model [20]. A full treatment of the analytical solution can be found in most texts on nuclear physics. The intent of the model is to analyze the dependence of single particle energy levels on deformation. In that spirit, our last check is to perform such an analysis numerically. Figure 6 depicts the results of single particle energy level calculations carried out on the collocation grid for a variety of Ω values and over a continuous range of deformation. For these calculations we used ninth-order splines and set the spin–orbit coupling at $\kappa = 0.05$. Comparison with standard "Nilsson plots" given in Refs. [21–23] indicate that we are in qualitative agreement.

VI. SUMMARY AND DISCUSSION

We have demonstrated that BSCM can be applied to eigenvalue problems with axial symmetry. The method allows for a simple treatment of boundary conditions along the symmetry axis. Further, we have shown that numerical calculations can be reduced to a quarter-plane by incorporating parity and setting boundary conditions in the equatorial plane. Finally, we have included strong spin–orbit coupling in the calculations. With the basic elements in place, the method can be applied to physically realistic models. In fact, using a deformed Woods–Saxon potential, we have been able to replicate many of the results reported in Ref. [24].

The successful use of highly nonlinear grid point distributions demonstrates that BSCM can be used to model weakly bound quantum states. It further suggests that low lying positive energy states may provide a reasonable approximation for the continuum. This would allow treatment of resonance phenomena.

TABLE IV

Fractional Error versus Spline Order M for $\Omega = \frac{3}{2}$, $\delta = 0.2$, $\kappa = 0$

Level	Eigenvalue	$M = 3$	$M = 5$	$M = 7$	$M = 9$
1	−31.275217	0.906E-03	0.173E-03	0.415E-05	0.610E-07
2	−25.005047	0.111E-02	0.961E-04	0.992E-06	0.381E-06
3	−23.480371	0.401E-02	0.457E-04	0.243E-04	0.406E-06
4	−18.734873	0.729E-02	0.357E-03	0.212E-04	0.143E-05
5	−17.210197	0.874E-02	0.113E-03	0.273E-04	0.332E-06
6	−15.685524	0.789E-02	0.126E-03	0.630E-04	0.936E-05

TABLE V

Fractional Error versus Spline Order M for $\Omega = \frac{3}{2}$, $\delta = 0$, $\kappa = 0.05$

Level	Eigenvalue	$M = 3$	$M = 5$	$M = 7$	$M = 9$
1	−32.527084	0.457E-03	0.120E-03	0.317E-05	0.117E-06
2	−25.751869	0.263E-03	0.187E-04	0.889E-06	0.222E-06
3	−23.968920	0.317E-02	0.294E-05	0.125E-04	0.159E-06
4	−18.976658	0.996E-02	0.507E-03	0.159E-04	0.804E-06
5	−18.263477	0.733E-02	0.196E-03	0.193E-04	0.386E-05
6	−16.480528	0.908E-02	0.375E-03	0.810E-06	0.347E-06

An important advantage of BSCM arises directly from the use of spline functions. The interpolating properties of splines lead naturally to a compact representation for both wavefunctions and operators. This in turn leads to a reduction in the numerical effort regardless of the particular method which is employed. Many of the comparisons which are presented in this paper are intended to illustrate that small increases in the interpolating order often lead to large gains in accuracy. This is significant in that the penalty which is incurred on the numerical effort as a result of increasing the spline order is generally much less than the penalty which would be incurred as a result of the grid refinement needed to obtain a similar increase in accuracy. As mentioned in Section II.B, in actual calculations one should check for convergence with respect to grid spacing as well as spline order. For large scale problems in which direct diagonalization is not practical, iterative techniques like damped gradient iteration may be used [25]. In such cases the ability to divide the Hamiltonian into several functional parts as shown in Eq. (22) represents a large reduction in the storage requirements for the operators. Although we have not done so, in principle it should be possible to further enhance the efficiency of iterative methods by exploiting the banded structure of the coefficient and operators matrices which appear in Section II.A.

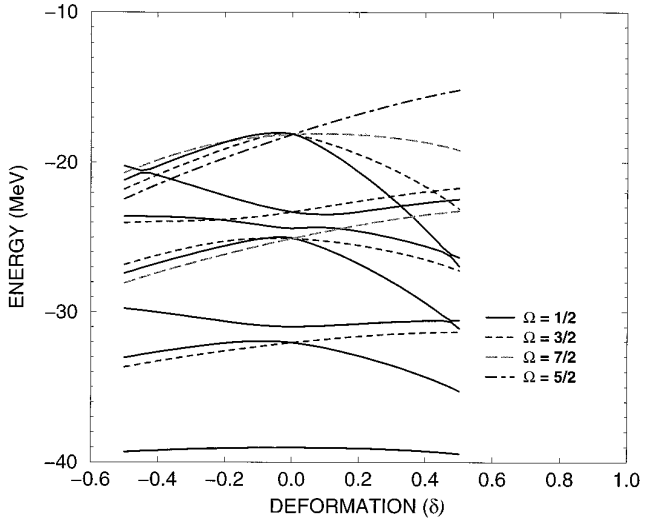

FIG. 6. Single particle energy levels as a function of deformation. Calculations were performed with BSCM using a grid partitioned uniformly with 1 fm knot segments in both dimensions. Oscillator parameters were selected to represent the states of a neutron in the field of a nucleus with mass number $A = 190$ and spin–orbit coupling $\kappa = 0.05$.

In reviewing the elements of the theory of the BSCM, we have emphasized the fact that most of the operations can be cast in matrix–vector form. The array processing features of FORTRAN 90 are particularly well suited for these operations. Several modules have been developed in conjunction with the present work, and they are available from the authors. In particular the module SPLINE90 is a compact collection of routines which can be used to generate B-splines for collocation or other applications.

ACKNOWLEDGMENTS

This research project was sponsored by the U.S. Department of Energy under Contract DE-FG05-87ER40376 with Vanderbilt University and under Contract DE-AC05-84OR21400 with Oak Ridge National Laboratory managed by Lockheed Martin Energy Systems, by the U.S. National Science Foundation through a grant for the Institute for Theoretical Atomic and Molecular Physics at Harvard University and the Smithsonian Astrophysical Observatory, and by the U.S. DOE High Performance Computing and Communications Program (HPCC) as the "Quantum Structure of Matter Grand Challenge" project. Professor Oberacker thanks the Institute for Nuclear Theory at the University of Washington for its hospitality and partial support during the completion of this work.

REFERENCES

1. D. Kincaid and W. Cheney, *Numerical Analysis* (Brooks/Cole, Belmont, CA, 1991).
2. T. N. E. Greville (Ed.), *Theory and Application of Spline Functions* (Academic Press, New York, 1969).
3. L. Schumaker, *Spline Functions: Basic Theory* (Wiley-Interscience, New York, 1980).
4. S. Singh, A. Carbine, R. Charron, and B. Watson, *Approximation Theory, Spline Functions and Applications* (Kluwer Academic, Dordrecht/Boston, 1992).
5. C. DeBoor, *A Practical Guide to Splines* (Springer-Verlag, New York/Berlin, 1978).
6. G. Nürnberger, *Approximation by Spline Functions* (Springer-Verlag, New York/Berlin, 1989).

7. R. E. Russel and L. F. Shampine, *Numer. Math.* **19,** 1 (1972).
8. A. S. Umar, J. Wu, M. R. Strayer, and C. Bottcher, *J. Comput. Phys.* **93,** 426 (1991).
9. The Fortran 90 Standard, ISO/IEC 1539:1991.
10. W. Nazarewicz, T. R. Werner, and J. Dobaczewski, *Phys. Rev. C* **50,** 2860 (1994).
11. C. F. Fischer and M. Idrees, *Comput. Phys.* **3,** 53 (1989).
12. R. L. Panton and H. B. Sallee, *Comput. Fluids* **3,** 257 (1975).
13. Kulander and Rescigno, *Comput. Phys. Commun.* **63,** 523 (1991).
14. W. Press, B. Flannery, S. Teukolsky, and W. Vetterling, *Numerical Recipes: The Art of Scientific Computing* (Cambridge Univ. Press, Cambridge, 1989).
15. E. Anderson *et al., LAPACK Users' Guide* (SIAM, Philadelphia, 1992).
16. C. Bottcher and M. Strayer, *Ann. Phys.* (*N.Y.*) **175,** 64 (1987).
17. C. A. J. Fletcher, *Computational Galerkin Methods* (Springer-Verlag, New York/Berlin, 1987).
18. B. W. Shore, *J. Chem. Phys.* **58,** 3855 (1973).
19. S. Flügge, *Practical Quantum Mechanics* (Springer-Verlag, New York/Berlin, 1994).
20. S. G. Nilsson, *Kgl. Dansk Videnskab Mat. Fys. Med.* **29** (1955).
21. P. Ring and P. Schuck, *The Nuclear Many-Body Problem* (Springer-Verlag, New York/Berlin, 1980).
22. J. M. Eisenberg and W. Greiner, *Nuclear Models,* Vol. 1 (North-Holland, Amsterdam, 1987).
23. J. Maruhn and W. Greiner, *Nuclear Models* (Springer-Verlag, New York/Berlin, 1995).
24. S. Cwiok, J. Dudek, W. Nazarewicz, J. Skalski, and T. Werner, *Comput. Phys. Commun.* **46,** 379 (1987).
25. A. S. Umar and M. R. Strayer, *Comput. Phys. Commun.* **63,** 179 (1991).